Feasibility study of a practical causal rate-independent damping device for the improved performance of seismic isolated structures

Zhanzhan Wu[a], Wei Liu[b], Kohju Ikago[b,*]

[a] *Graduate School of Engineering, Tohoku University, Sendai 980-8572, Japan*
[b] *International Research Institute of Disaster Science, Tohoku University, Sendai 980-8572, Japan*

Abstract

When rate-independent linear damping (RILD) is incorporated into a base-isolated structure, it achieves a similar response displacement reduction effect with significantly lower floor response acceleration compared with linear viscous damping (LVD) with the same loss factor. To address the undesirable stiffness added to an isolation layer when we adopt a mechanical device comprising a few branches of a spring-dashpot link to realize RILD, this study proposes canceling the undesirable isolator stiffness by adding an inerter element and reducing the isolator stiffness. A heuristic optimization method was developed to design the proposed mechanical device to mimic the behavior of RILD. A parametric survey on the optimal designs of the device suggests that the three branches of the spring-dashpot link work best in terms of practicality and feasibility. Seismic control performance was assessed using a 10-story base-isolated building mounted on linear and nonlinear isolation systems. Analyses of linear systems revealed that the proposed device achieved lower inter-story drifts and approximately 40% reduction in floor response acceleration with a 4% increase in isolator displacement compared with the LVD when subjected to high-frequency ground motions. Analyses of the nonlinear systems showed that the displacement control performance of the proposed model was slightly compromised when subjected to ground motions dominated by low-frequency components, thereby identifying a further challenge in developing a causal RILD device for nonlinear structures.

Keywords: rate-independent linear damping, Maxwell-Wiechert model, inerter, low-frequency structure, global optimization algorithm

*Corresponding author
468-1, Aramaki Aza-Aoba, Aoba-ku, Sendai 980-8572, Japan
Email addresses: wu.zhanzhan.p5@dc.tohoku.ac.jp (Zhanzhan Wu), wei.liu.b4@tohoku.ac.jp (Wei Liu), ikago@irides.tohoku.ac.jp (Kohju Ikago)

1. Introduction

The 2011 Great East Japan Earthquake caused many low-frequency structures, such as base-isolated and high-rise buildings (previously considered safe), to suffer from excessive displacement and long-duration vibrations, causing interior and exterior damage [1]. Consequently, the protection of low-frequency structures, including their nonstructural components, from low-frequency ground motion induced by massive earthquakes is attracting increasing attention from engineers and researchers.

Adopting conventional energy dissipators, such as viscous and hysteretic dampers(HDs), may be ineffective in mitigating excessive displacement in base-isolated structures. A viscous damper can generate insufficient control force against low-frequency vibration, whereas the maximum resistive force of an HD is constant, irrespective of the response displacement, thereby resulting in a decreased equivalent damping ratio for excessive displacement. Magnetorheological dampers can provide an adaptive control force [2] but may fail during strong earthquakes. Thus, there is a need for alternative approaches that use a passive system that does not require an external power source, is unconditionally stable, and is easy to maintain. Rate-independent linear damping (RILD), also referred to as structural damping, complex-valued stiffness, and linear or ideal hysteretic damping [3, 4, 5, 6] is an attractive option that provides effective damping performance when incorporated into base-isolated structures [7].

The idea of RILD was first proposed to represent the damping properties of materials, such as metals and soils, whose energy loss per cycle is independent of the frequency over a wide frequency range [8, 9]. The resistive force of the RILD is in phase with the velocity, resulting in energy dissipation, whereas its amplitude is proportional to the response displacement, thus enabling the direct control of the total displacement [10]. Nonetheless, RILD is a physically unsound mathematical model that cannot be realized using a real-life device owing to its non-causality (i.e., it exhibits a response even when no excitation is applied), as discussed in references [6, 8, 11, 12].

To address the non-causality challenge, various causal RILD models have been examined in previous studies. The first successful causal model was proposed by Biot [13] and consists of infinite Maxwell elements. Reducing computational costs in the time domain of systems incorporating the Biot model has also been pursued [9, 14, 15, 16]. Makris [17] proposed a causal RILD

model by adding a frequency-dependent real part to the dynamic stiffness to satisfy the causality requirement, thereby suggesting that a causal RILD model can be achieved at the expense of increasing the storage stiffness. Later, Muravskii [18] constructed a causal linear damping model with nearly frequency-independent dynamic stiffness in the time and frequency domains, by entirely considering the structural system. Nakamura [19] proposed a causal model with constant loss stiffness over a series of piecewise frequency ranges using causally approximated impulse responses of the imaginary unit function. Recently, Huang [20] presented a practical algorithm that provides frequency-independent loss stiffness over the frequency range of interest. These causal RILD models can mimic the constant-loss stiffness characteristics of an ideal model, although physical realization is difficult.

The tuned Maxwell–Wiechert (TMW) model proposed by Genta and Amanti [21] is a viable option for physically realizing RILD with a minimum number of mechanical components. A TMW model comprises a finite number of branches, whose relaxation parameters are distributed in a geometric progression. The loss stiffness is nearly constant over a specified frequency range. Another notable causal model was established by Luo and Ikago [7], who built a mechanical model comprising a linear negative-stiffness element coupled in parallel with a Maxwell element, which is a mechanical realization of the causal approximation RILD method (called a first-order all-pass filter that has a constant gain over all frequencies and a 90° degree phase advance at a prescribed frequency) proposed by Keivan et al. [22].

A series of dynamic tests [23, 24, 25, 26, 27] have validated the performance of the passive RILD model developed by Luo and Ikago [7]. In particular, Liu and Ikago [24] indicated that the inherent friction in the device components must be considered to further improve the accuracy of the analytical model of the devices. Luo and Ikago [28] proposed a theory that connects causal RILD models developed by independent researchers in a unified manner by extending the first-order filter to fractional orders.

Previous studies on causal RILD models mainly focused on loss stiffness and paid less attention to storage stiffness [27]. The application of causal RILD to exploit its benefits in improving the performance of a base-isolated structure, a large undesirable storage stiffness that compromises the flexibility of the isolators may be present. In this study, we aimed to explore causal mechanical models that achieve a constant loss stiffness and near-zero storage stiffness over a specified frequency range.

To achieve this goal, a causal mechanical model consisting of a negative-stiffness element, inerter, and TMW model is proposed, as shown in Fig. 1). The proposed model is designed in two stages. First, a TMW model with multiple branches that exhibits frequency-independent loss of stiffness over a specified frequency range was designed. Subsequently, the values of the negative stiffness and inerter elements that ensure zero stiffness at the two specified frequencies were determined.

The proposed model can be constructed using a combination of readily available devices or can be obtained by making slight modifications. For example, Maxwell elements can be realized using a combination of laminated rubber and a fluid damper connected in series. A viable option for inerter elements is the rotary inerter damper, developed by Nakaminami et al. [29] (Fig. 2), which can accommodate sufficient inertance and stroke to control seismically isolated structures. The maximum inertance and stroke of this device are 1250 tons and 0.6 m, respectively. Experimental validation on a full-scale inerter device was conducted by Watanabe et al. [30] No special device is required to realize the negative-stiffness element because reducing the horizontal stiffness of the isolation layer by $|k_n|(< k_0)$ is equivalent to adding a negative-stiffness element.

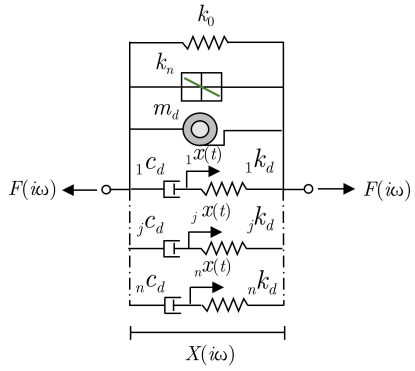

Figure 1: Proposed model

The novelty of this study lies in providing an effective means to eliminate undesirable storage stiffness to maintain isolator flexibility, proposing a heuristic method for finding the optimal relaxation parameters for TMW, and identifying a challenge that remains in the proposed system when it is incorporated into a nonlinear system. The optimum design of the proposed system has practically constant loss stiffness and near-zero storage stiffness within a specified frequency range, achieving simultaneous reductions in displacement and floor response acceleration in a base-isolated structure.

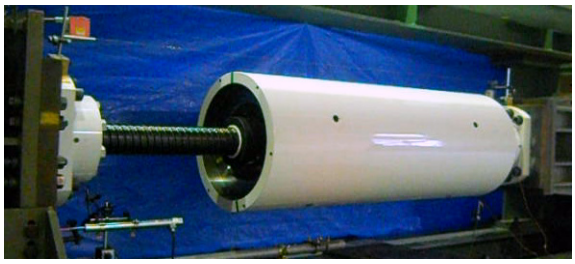

Figure 2: Rotary inerter damper (Nakaminami et al. [29])

The remainder of this paper is organized as follows. Section 2 presents a brief review of causal RILD models. In Section 3, a literature review is provided, mathematical expressions of the proposed model are derived, and the parameter design process is presented, followed by identification of the appropriate number of branches of Maxwell elements. Finally, the proposed model was compared with other causal RILD models. Section 4 discusses and demonstrates the efficiency of the proposed device in improving the performance of a base-isolated structure through numerical analysis of linear and nonlinear isolation systems. Finally, Section 5 concludes the paper.

2. Mathematical models for RILD

This section provides a brief review of the RILD models. The damping functions of the ideal RILD, Biot, Makris, and TMW models were presented.

2.1. Ideal RILD

Let $X(i\omega)$ be the displacement in the frequency domain at the angular frequency ω, where $i = \sqrt{-1}$ is the imaginary unit. Subsequently, the velocity was expressed as $i\omega X(i\omega)$. This implies that the velocity depends on the frequency, and its phase is 90° advanced to the displacement. Here, we consider a signal whose amplitude is independent of frequency and whose phase is advanced by 90°, which is a Hilbert transform of displacement. The mathematical expression is $i\mathrm{sgn}(\omega)X(i\omega)$, where sgn( ) denotes the signum function.

The resistive force of a RILD element is proportional to displacement, independent of frequency, in phase with velocity; thus, it can be expressed as $k_L i\mathrm{sgn}(\omega)X(i\omega)$, where the real value k_L, designated as the loss stiffness, has a dimension of stiffness.

Arranging a real-valued linear stiffness k_0 and a RILD element in parallel yields complex-valued stiffness, as shown in Fig. 3(a). The force-deformation relationship in the frequency domain is

$$F(i\omega) = [k_0 + ik_L \mathrm{sgn}(\omega)]X(i\omega) = k_0[1 + i\eta \mathrm{sgn}(\omega)]X(i\omega) = k_0[1 + {}_{\mathrm{R}}\mathcal{Q}(i\omega)]X(i\omega). \tag{1}$$

where $\eta = k_L/k_0$ and ${}_{\mathrm{R}}\mathcal{Q}(i\omega)$ (the left subscript R is the first letter of the RILD element) represent the loss factor and damping function of the RILD element, respectively.

The coefficient $k_0[1 + {}_{\mathrm{R}}\mathcal{Q}(i\omega)]$ as the ratio of the resistive force to the displacement is referred to as the dynamic stiffness. The real and imaginary parts of the dynamic stiffness are referred to as the storage and loss stiffnesses, respectively. The storage stiffness k_0 has the same meaning as the conventional stiffness, whereas the loss stiffness $k_L \mathrm{sgn}(\omega) = \eta k_0 \mathrm{sgn}(\omega) = \mathrm{Im}[k_0 \, {}_{\mathrm{R}}\mathcal{Q}(i\omega)]$ is related to energy loss or dissipation.

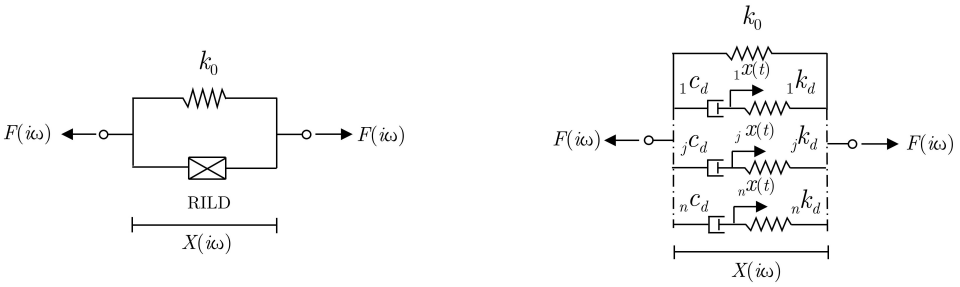

(a) Complex-valued spring

(b) Maxwell-Wiechert model

Figure 3: Noncausal and causal models

2.2. Biot model

The damping function of a Biot model with loss factor η can be expressed as [9]

$${}_{\mathrm{B}}\mathcal{Q}(i\omega) = \frac{2\eta}{\pi}\left[\ln\sqrt{1 + \left(\frac{\omega}{\varepsilon}\right)^2} + i\arctan\left(\frac{\omega}{\varepsilon}\right)\right], \tag{2}$$

where ε is an arbitrary positive real number and subscript B is the first letter of the Biot model.

2.3. Makris model

The damping function of the Makris model, ${}_{\mathrm{M}}\mathcal{Q}(i\omega)$ is [17]

$${}_{\mathrm{M}}\mathcal{Q}(i\omega) = \frac{2\eta}{\pi}\ln\left|\frac{\omega}{\varepsilon}\right| + i\eta \mathrm{sgn}(\omega) \tag{3}$$

where subscript M is the first letter of the Makris model. This provides insight into the causal approximation of RILD; the accuracy in loss stiffness is ensured at the expense of the addition of undesirable storage stiffness, which is proportional to the logarithm of the frequency.

2.4. Tuned Maxwell–Wiechert model

The TMW model [21, 31] is one of the most viable options for developing a physical device using a minimum number of mechanical components. Assume a TMW model contains n branches of Maxwell elements in which the stiffness and relaxation time of the j-th branch are ${}_j\eta_m k_0$ and $\tau_j = 2\pi/\beta_j$, respectively, as shown in Fig. 3(b). The damping function, ${}_{\mathrm{T}}\mathcal{Q}$ is

$$ {}_{\mathrm{T}}\mathcal{Q}(i\omega) = \sum_{j=1}^{n} \frac{i\omega}{i\omega + \beta_j} {}_j\eta_m, \tag{4} $$

where subscript T is the first letter of the TMW model. $\beta_j = {}_j k_d / {}_j c_d$ is the angular frequency derived from relaxation time τ_j, which is designated as a relaxation parameter.

3. Modified TMW model

This section develops an energy dissipation device for a seismically isolated structure that effectively reduces isolator displacement without compromising the floor response acceleration. Such control performance can be achieved using a device that selectively dampens low-frequency vibration components. The development of the device proposed in this study is inspired by the constant-loss stiffness characteristics with zero storage stiffness obtained from ideal RILD characteristics.

As Makris [17] demonstrated, adding undesirable storage stiffness is necessary to ensure the causality of RILD. However, the loss stiffness becomes nearly proportional to the frequency in an attempt to ensure zero storage stiffness.

The proposed model is based on the TMW model, which has the inherent drawback of adding undesirable storage stiffness in the frequency region, where its loss stiffness is nearly constant. We used a constant negative stiffness element and an inerter element to reduce the undesirable storage stiffness to maintain isolator flexibility. Combining the two types of negative-stiffness elements enables us to adjust the storage stiffness of the isolation layer to at least two specified frequencies. Adding an inerter device provides negative stiffness proportional to the frequency's square, whereas reducing the isolator stiffness by replacing rubber isolators with sliders can achieve constant negative stiffness.

The most straightforward way to realize constant negative stiffness is to reduce the isolator stiffness by replacing the rubber isolators with sliders, such that the horizontal stiffness of the isolation layer is reduced from k_0 to $k_0 + k_n$ as discussed by Luo and Ikago[7]. Another option is to use mechanical negative-stiffness devices developed by Sarlis et al. [32, 33] and Sun et al. [34]. Luo and Ikago [7] further discussed the nonlinear effects of these devices when incorporated into a seismic isolation layer along with a Maxwell element.

3.1. Definitions and formulations of inerter-negative stiffness-TMW model

The proposed system is designated as the inerter-negative stiffness-tuned Maxwell–Wiechert (INSTMW) model (Fig. 1) [35]. The terms related to the resistive forces generated by the inerter and negative stiffness are added to Eq. (4) to yield the following damping function for the proposed system.

$$ {}_{\mathrm{I}}\mathcal{Q}(i\omega) = -\mu\omega^2 + \eta_n + \sum_{j=1}^{n} {}_j\eta_m \frac{i\omega}{i\omega + \beta_j}, \tag{5}$$

where the subscript I is the first letter of the INSTMW model. $\mu = m_d/k_0$ represents the ratio of inertance m_d to the stiffness k_0. $\eta_n = k_n/k_0 (< 0)$ is the ratio between the negative stiffness $k_n (< 0)$ and the positive stiffness k_0.

By separating the real and imaginary parts of the damping function, we obtain:

$$ \mathrm{Re}\left[{}_{\mathrm{I}}\mathcal{Q}(\omega)\right] = -\mu\omega^2 + \eta_n + \sum_{j=1}^{n} \frac{\omega^2 {}_j\eta_m}{\omega^2 + \beta_j^2}, \tag{6}$$

$$ \mathrm{Im}\left[{}_{\mathrm{I}}\mathcal{Q}(\omega)\right] = \sum_{j=1}^{n} \frac{\omega \ {}_j\eta_m \ \beta_j}{\omega^2 + \beta_j^2}. \tag{7}$$

The inerter and negative stiffness elements modify the storage stiffness without affecting the loss stiffness because they do not dissipate energy. Eq. (6) suggests that the real part of the normalized damping function approaches $\eta_n (< 0)$ and $-\infty$ when the excitation frequency approaches zero and ∞, respectively. This implies that the storage stiffness of the proposed model can be negative in low- and high-frequency ranges. However, the storage stiffness of the TMW portion dominates, and the total storage stiffness becomes positive in the intermediate-frequency range. The storage stiffness can be adjusted to zero at the two distinct frequencies. Thus, the proposed model is expected to satisfy the requirements for the desired device such that it exhibits a rate-independent damping property with only moderate changes in storage stiffness over the frequency range of interest.

3.2. Optimization of the proposed model

Makris and Zhang [14] identified the stiffness values and relaxation parameters in Maxwell–Wiechert models using nonlinear regression. Spanos and Tsavachidis [15] proposed a recursive algorithm to obtain an approximate damping kernel function for the Biot model using Prony's method. Liu and Ikago [27] used the fundamental natural frequencies of a control structure as the target frequencies at which the loss stiffness should be adjusted. Another Maxwell–Wiechert model-based method for approximating a given damping ratio distribution by using a proportional damping model was proposed by Lee [36].

The proposed system is designed in two stages. In the first stage, the parameters of a TMW model, whose loss stiffness is approximately constant over a specified angular frequency range, are determined. A heuristic approach is then adopted to determine the parameters; nonetheless, any existing method is applicable.

In the second stage, the constant negative stiffness and inertance are determined such that the proposed system has zero storage stiffness at the two specified frequencies, defining the frequency range of interest.

Step 1: TMW parameter identification

An optimum design problem was established to determine the parameters of the TMW model that provide a constant loss stiffness over a specified angular frequency range. The number of Maxwell branches in the TMW model was n. Let the lower and upper bounds of the specified angular frequency range be ω_s and ω_e, respectively. When the angular frequency range $[\omega_s, \omega_e]$ is divided into N segments with a uniform interval $\Delta\omega = (\omega_s - \omega_e)/N$, a series of discrete angular frequencies $\omega_\ell = \omega_s + \ell\Delta\omega$ $(\ell = 0, 1, 2, \cdots, N)$ can be defined. The parameters of the TMW are sought such that the square root of the sum of the errors at frequencies ω_ℓ is minimized. Thus, the

optimum design problem is formulated as follows.

$$\begin{aligned}
&\text{find}: \ {}_j k_d, \ {}_j c_d \quad (j = 0, 1, 2, \cdots, n) \\
&\text{to minimize}: f_{obj} = \frac{1}{\eta}\sqrt{\frac{1}{N+1}\sum_{\ell=0}^{N}\left(\mathrm{Im}\left[{}_{\mathrm{I}}\mathcal{Q}(i\omega_\ell)\right] - \eta\right)^2} \\
&\text{subject to}: \\
&\qquad {}_j k_d^{\min} \le {}_j k_d \le {}_j k_d^{\max} \\
&\qquad {}_j c_d^{\min} \le {}_j c_d \le {}_j c_d^{\max},
\end{aligned} \tag{8}$$

where ${}_j k_d^{\min}$,${}_j c_d^{\min}$,${}_j k_d^{\max}$,${}_j c_d^{\max}$ are the lower and upper bounds of design variables, respectively.

Step 2: Design of constant negative stiffness and inerter

A set of simultaneous linear equations involving two unknown parameters (μ and η_n) is derived from the zero-storage stiffness condition at two specified angular frequencies, $\hat{\omega}_1$ and $\hat{\omega}_2$.

$$\mathrm{Re}\left[{}_{\mathrm{I}}\mathcal{Q}(i\omega)\right]_{\omega=\hat{\omega}_1,\hat{\omega}_2} = 0. \tag{9}$$

Substituting Eq. (6) into Eqs. (9) yields

$$-\mu\omega^2 + \eta_n + \sum_{j=1}^{n}\frac{\omega^2 {}_j\eta_m}{\omega^2 + \beta_j^2} = 0, \quad \text{for } \omega = \hat{\omega}_1 \text{ and } \hat{\omega}_2. \tag{10}$$

The storage stiffness at zero frequency is.

$$k_0 \mathrm{Re}\left[{}_{\mathrm{I}}\mathcal{Q}(0)\right] = \eta_n k_0 = k_n. \tag{11}$$

To ensure positive static stiffness for the entire system, the absolute value of the negative stiffness $|k_n| = |\eta_n k_0|$ cannot exceed k_0.

3.3. Particle Swarm Optimization

Many options can be used, including gradient-based and metaheuristic approaches. For example, particle swarm optimization (PSO) [37, 38, 39] is a population-based metaheuristic optimization technique that can solve complicated mathematical problems without information regarding the gradient and Hessian of the objective function. It also has other advantages, including insensitivity to design variable scaling, fast convergence, high efficiency, and ease of implementation. Among the many PSO variants, PSO with a linearly decreasing inertia weight is the most used; thus,

we adopted it to solve the optimum design problem in this study. Appropriately adjusting the individual and swarm best positions may be a viable alternative method for improving the ability of PSO to search for global optima [40]. A brief introduction to PSO is provided below for reference purposes.

The position of an individual candidate solution (designated as a particle) is directly influenced by its best position and the best position of the population of candidate solutions (designated as a swarm) at each iteration step; it is also affected by three critical parameters: inertia weight factor, cognitive parameter, and social parameter. Adjusting the value of the inertia weight factor can prompt particles to have a greater tendency to move toward and explore the area with the best objective value. Generally, higher values result in strong global search capability, whereas the opposite holds for the local search capability. To ensure an efficient search, the dynamic inertia weight was determined such that it decreased linearly [38], as presented in Eq. (12).

$$w_p = (w_i - w_f)\frac{G_{max} - p}{G_{max}} + w_i. \tag{12}$$

where w_p denotes the inertial weight at the pth step. w_i and w_f represent the inertial weights in the initial and final steps, respectively. G_{max} denotes the maximum number of iterations. Regarding the cognitive and social parameters, these two weigh the importance of the best previous experiences of individual particles and global swarm. The iterative PSO process is illustrated in Fig. 4 (step 1). The entire search process is illustrated in Fig. 4. Step 2 must be performed after completing Step 1. The PSO parameters adopted in this study are listed in Table 1.

It is impossible to obtain a constant loss stiffness near the zero-frequency region using the TMW model. However, it is important to consider the low-frequency components in this study. Thus, the lower bound of the angular frequency range ω_s is chosen as 0.5 rad/s. Another critical parameter applied in the optimization process is the angular frequency interval $\Delta\omega$, which has a nonnegligible influence on the accuracy of the approximation. A small value of $\Delta\omega$ ensures accuracy at the expense of the computational burden. Conversely, a high value guarantees a faster calculation at the expense of accuracy. An empirically obtained angular frequency increment of 0.05 rad/s is adopted in this study, as it can ensure practically acceptable accuracy and reasonable computational demand.

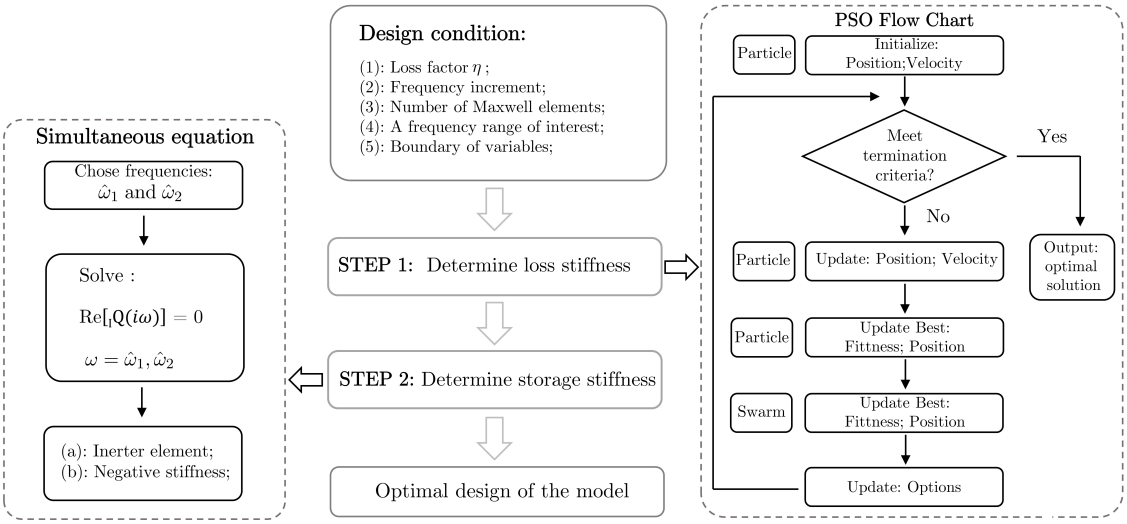

Figure 4: Flow chart of the design procedure

3.4. Number of branches and target frequency range

The effectiveness of the TMW model in achieving constant loss stiffness is directly affected by the number of branches and also influenced by the width of the target angular frequency range ($\omega_e - \omega_s$). A wider target frequency range may require a larger number of branches. Whereas a narrow range may compromise the overall performance. This poses the following questions:

(1) What is the appropriate target frequency range for a TMW model that uses a minimum number of branches?

(2) How many Maxwell elements are required to ensure practically acceptable accuracy when approximating constant loss stiffness in the target frequency range?

To address these two questions, a parametric survey of TMW models was conducted. Table 2 presents the parameters used.

Let the optimum design be ${}_jk_d^o, {}_jc_d^o$. Further, let ${}_j\eta_m^o = {}_j\ k_d^o/k_0$ and $\beta_j^o = {}_jk_d^o/{}_jc_d^o$. The mean values ($\bar{\eta}$) and coefficients of variation (CV) of the loss factors of the optimally designed TMW

Table 1: PSO parameters

Parameter description	Value
Inertia weight $[w_i;\ w_f]$	[0.9; 0.4]
Cognitive parameter	0.5
Social parameter	1.5
Population size	200
Maximum generation $G_{\max}$	500
Number of design parameters	$2n$
Tolerance function	10^{-6}
Frequency interval $\Delta\omega$ (rad/s)	0.05

models are defined as follows.

$$\bar{\eta} = \frac{1}{N+1}\sum_{\ell=0}^{N}\sum_{j=1}^{n}\frac{\omega_{\ell j}\eta_m^o\beta_j^o}{\omega_\ell^2+\beta_j^{o2}}, \tag{13}$$

$$CV = \frac{1}{\bar{\eta}}\sqrt{\frac{1}{N+1}\sum_{\ell=0}^{N}\left(\sum_{j=1}^{n}\frac{\omega_{\ell j}\eta_m^o\beta_j^o}{\omega_\ell^2+\beta_j^{o2}}-\bar{\eta}\right)^2}. \tag{14}$$

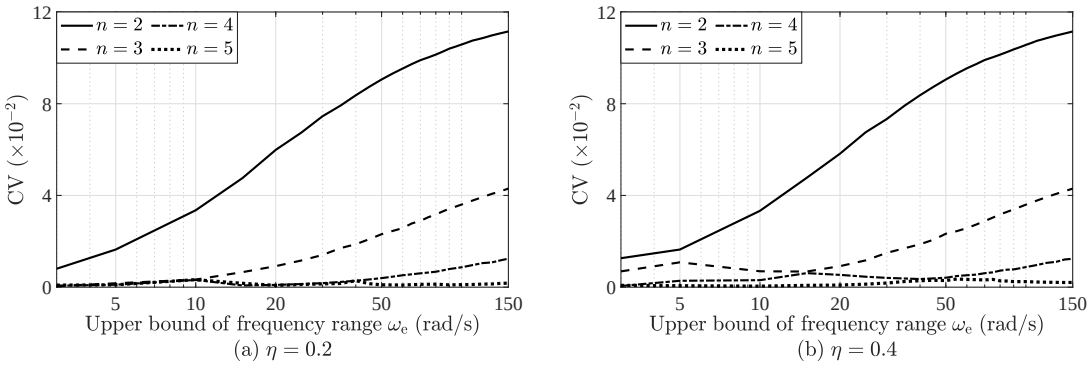

Figure 5: Coefficients of variation of optimally designed TMW models with n branches

The CV values are close to those obtained with the objective function f_{obj} defined in Eq. (8). The difference between CV and f_{obj} is that $\bar{\eta}$ in Eq. (14) is not equal to the target loss factor, η.

Fig. 5 shows the relationship between the upper bound frequencies ω_e and CV. Increasing the

Table 2: Parameters used in the parametric survey

Parameter description	Value
Number of branches n	2, 3, 4, 5
Lower bound of target angular frequency range ω_s [rad/s]	0.5
Upper bound of target angular frequency range ω_e [rad/s]	0.5∼150
Target loss factor	0.2, 0.4
${}_jk_d^{\min}$ [kN/m]	0
${}_jk_d^{\max}$ [kN/m]	k_0
${}_jc_d^{\min}$ [kN·s/m]	0
${}_jc_d^{\max}$ [kN·s/m]	$\tau_{max}k_0/2\pi$
Maximum relaxation time $\tau_{\max}$ [s]	4.0

number of branches n from 2 to 3 reduces the approximation error. CV increases as the upper-bound frequency increases when ω_e is greater than 50 rad/s for cases $n =$ 2, 3, and 4.

Considering the trade-off between the acceptable accuracy and simplicity of the model, we determined the number of branches and the upper bound angular frequency to be $n = 3$ and $\omega_e = 50$ rad/s, respectively. An upper-bound angular frequency of 50 rad/s was selected because angular frequencies higher than 50 rad/s have a minimal effect on the model's response.

3.5. Comparison of causal RILD models

The INSTMW model was compared with the TMW, Biot, Makris, and RILD models, with the same target loss factor of $\eta = 0.4$. The number of branches and the target angular frequency range of the INSTMW and TMW models were $n = 3$ and [0.5, 50] rad/s, respectively. The other PSO parameters used to determine the stiffness values and damping coefficients of the Maxwell elements are the same as those listed in Table 1. The first and second natural angular frequencies $\hat{\omega}_1 = 1.57$ and $\hat{\omega}_2 = 13.57$ rad/s of the base-isolated structure example introduced in the next section were employed as the target frequencies to determine the inertance and negative stiffness of the INSTMW model. Following suggestions in the literature[9, 12, 14] , $\varepsilon = \hat{\omega}_1/10$ was used as a practical choice for the Biot model, whereas $\varepsilon = \hat{\omega}_1$ was used for the Makris model, such that it had the same dynamic stiffness at the frequency $\hat{\omega}_1$.

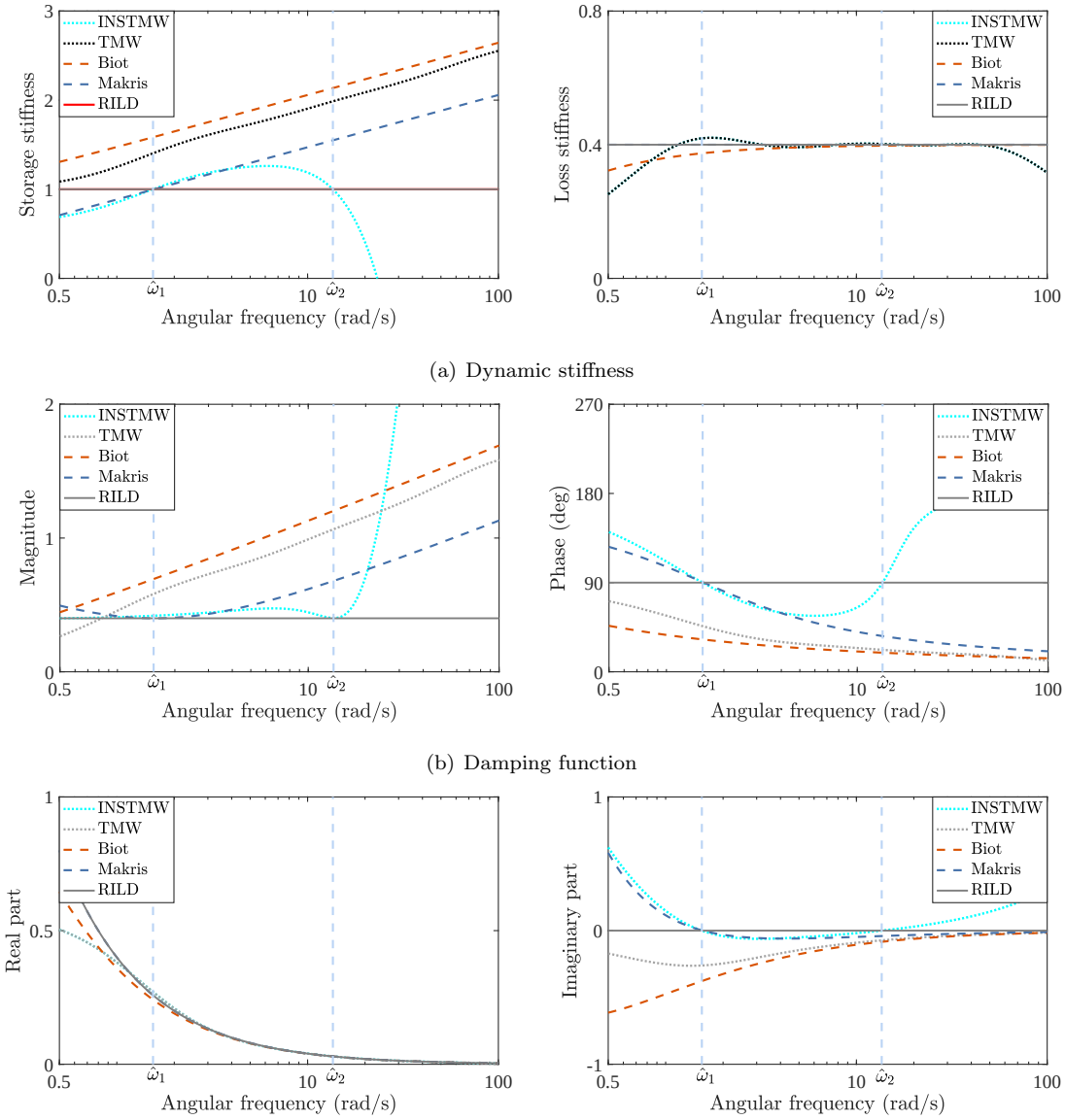

(a) Dynamic stiffness

(b) Damping function

(c) Impedance function

Figure 6: Comparison of properties among different causal damping models and RILD

Fig. 6 shows the dynamic stiffness, damping function, and impedance function (transfer function from the velocity to the damping force) of the different damping models. The Biot model has a frequency-insensitive loss stiffness over the range $\omega > \hat{\omega}_1$. The INSTMW and TMW models exhibit

practically constant loss stiffness in the target frequency range as intended, whereas considerable differences appear in the storage stiffness. The storage stiffness values of the Biot and TMW models were significantly higher than those of competing models. The storage stiffness of INSTMW is identical to that of RILD at the two specified frequencies as intended. However, it decreases rapidly over the region $\omega > \hat{\omega}_2$ and falls below zero at approximately 30 rad/s, owing to the inerter element effect.

Fig. 6(b) indicates that the magnitude of the damping function of the INSTMW model is similar to that of RILD over the angular frequency range $\omega < \hat{\omega}_2$. Moreover, the phase of its damping function is closer to that of RILD than either the TMW or Biot models. Fig. 6(c) shows that the real parts of the impedance functions of the TMW-based models disagree with those of RILD in the low-frequency range, whereas those of the Biot and Makris models agree well with RILD over a broad frequency region. As for the imaginary parts of the impedance functions, the INSTMW and Makris models show good agreement with RILD in the specified angular frequency range.

Thus, these results demonstrate that the INSTMW model can achieve the desired frequency-independent loss stiffness over the specified frequency range while improving the storage stiffness compared to other causal RILD models.

4. Design example of INSTMW device for a multi-story base-isolated structure

This section presents a design example of an INSTMW device for a 10-story base-isolated building. The performance of the proposed device was compared with those of the TMW, LVD, and RILD models. A case in which all the components in the base-isolated building, including the damping devices, are linear is discussed, followed by a case study in which an HD is incorporated into the isolation layer.

4.1. Base-isolated building structure

The seismic response control performances of the proposed and other damping models were examined using a 10-story base-isolated building model, as shown in Fig. 7. The superstructure is a shear building, and its fundamental natural period is 0.8 s when its base is fixed. As reported by Ryan and Polanco [41] and Anajafi, Medina, and Santini-Bell [42], mass-proportional damping can lead to an underestimated seismic response. Thus, stiffness proportional damping is considered, with an inherent damping ratio of 3% assigned to the first mode of the superstructure when its base

is fixed following recommendations in the literature [41, 42] The isolator stiffness k_0 is determined such that the fundamental natural period of the entire system is 4.0 s. The inherent damping in the isolation layer was neglected. Tables 3 and 4 list the specifications and modal parameters of the 10-story base-isolated model.

Here, all model components, including the superstructure, isolator, and damping devices, are assumed to exhibit linear responses under seismic excitation. Nonetheless, the seismic performance of the proposed model under nonlinear conditions should be examined. Hybrid damper systems with an HD are common in practice. In addition, combining an HD with a base-isolation layer offers two advantages: controlling the isolator displacement induced by the static component representing the wind load and providing a fail-safe mechanism when the linear damping system fails. Thus, HD is introduced in the base-isolation layer to provide nonlinearity to the system.

For simplicity, HD was assumed to be a perfect elastoplastic material with a yield displacement of 0.03 m. The yield load coefficient α is defined as the ratio of the yielding load to the total weight of the superstructure, including the base mass. The yielding load was determined such that the HD remained elastic for a 500-year wind load return period. Thus, the yield load coefficient α was determined as 3.2%.

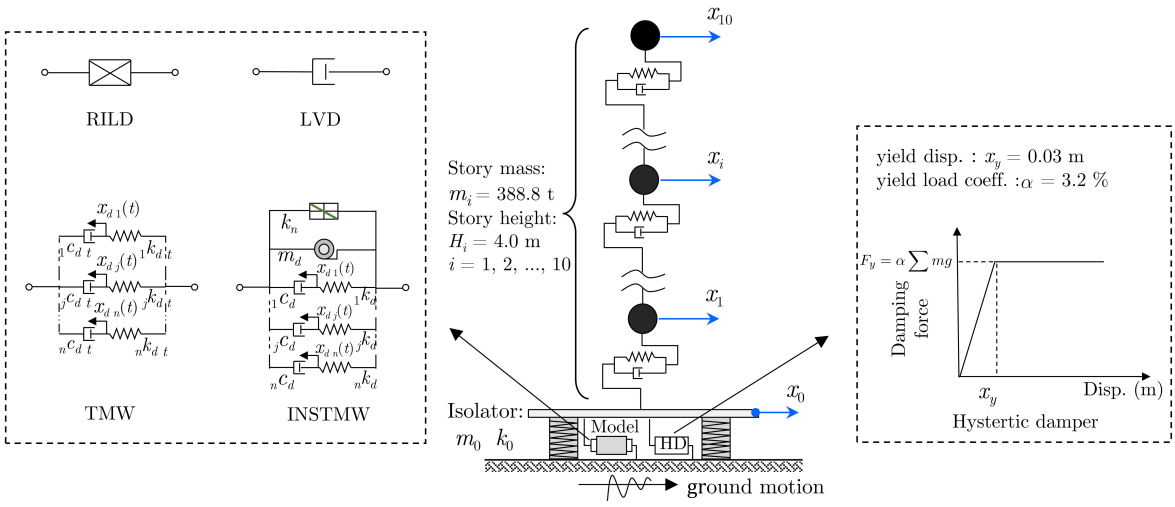

Figure 7: Basic 10-story base-isolated structure equipped with different damping models

Table 3: Specifications of the 10-story base-isolated building

Story #	Base(0)	1	2	3	4	5	6	7	8	9	10
Mass m_i (ton)	388.8	388.8	388.8	388.8	388.8	388.8	388.8	388.8	388.8	388.8	388.8
Stiffness $k_{i,s}$($\times 10^3$ kN/m)	10.6	1400	1296.3	1192.6	1088.9	985.2	881.5	777.8	674.1	570.4	467.7
Damping $c_{i,s}$(kN·s/m)	0	11247	10414	9581	8748	7914	7081	6248	5415	4582	3749
Height (m)	2.73	4.0	4.0	4.0	4.0	4.0	4.0	4.0	4.0	4.0	4.0

Table 4: Modal parameters of the 10-story base-isolated building

Mode number	1	2	3	4	5	6	7	8	9	10	11
Frequency (rad/s)	1.57	13.6	26.3	38.5	49.9	60.1	69.2	77.8	86.8	96.8	108.8
Modal damping ratio (%)	0.59	5.20	10.08	14.77	19.13	23.04	26.53	29.85	33.30	37.13	41.72

4.2. Historic ground motions

Four seismic records with different magnitudes were selected. The first two are near-fault pulse-like ground motions that can cause considerable structural damage owing to their excessively strong velocity pulses: (1) the North–South component of the 1995 Kobe Earthquake recorded at the Japan Meteorological Agency at Kobe (hereinafter referred to as the 1995 Kobe N–S record) and (2) the North–South component of the 1994 Northridge Earthquake recorded at the Sylmar Country Hospital (SCH) (hereinafter referred to as the 1994 Northridge SCH record). The other two are long-duration ground motions and contain abundant low-frequency components: (3) the North–South component of the 1968 Tokachi-oki Earthquake recorded at the Hachinohe Harbor (hereinafter referred to as the 1968 Hachinohe N–S) and (4) the 2011 Great East Japan Earthquake recorded at Tohoku University N–S (hereinafter referred to as the 2011 Tohoku N–S record). Table 5 lists the detailed properties of these four seismic records. Fig. 8 shows the acceleration time history.

4.3. Equations of motion

Consider a superstructure with n stories ($n = 10$ in this study) mounted on a BIS containing supplemental damping devices. The base mass, isolator stiffness, and isolator displacement were m_0, k_0, and x_0, respectively, as shown in Fig. 7. The equations of motion for the base-isolated structure equipped with supplemental damping models when subjected to ground acceleration $\ddot{x}_g$

Table 5: List of ground motions used in this study

Seismic records	Magnitude	Duration (s)	PGA (cm/s^2)	PGV (cm/s)
1995 Kobe N–S	6.9	20	818	91
1994 Northridge SCH	6.7	20	826	129
1968 Hachinohe N–S	7.9	234	231	33
2011 Tohoku N–S	9.0	250	333	50

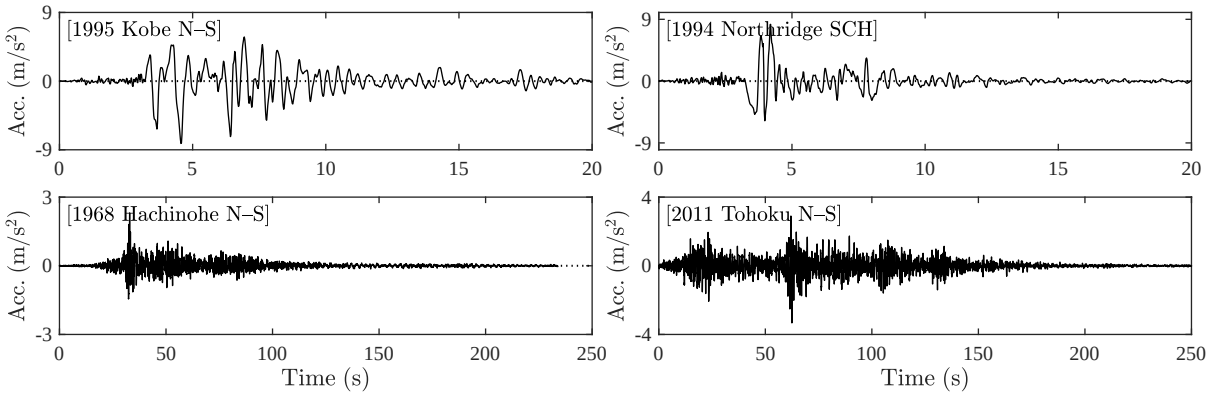

Figure 8: Time-histories of the selected ground motions

are expressed as follows:

$$\mathbf{M}\ddot{\mathbf{x}} + \mathbf{C}\dot{\mathbf{x}} + \mathbf{K}\mathbf{x} + \boldsymbol{\phi_d} F_d + \boldsymbol{\phi_h} F_{\mathrm{HD}} = -\mathbf{M}\boldsymbol{\phi}\ddot{x}_g, \tag{15}$$

where $\mathbf{x} = [x_0, x_1, \cdots, x_n]^T$, $\mathbf{M} = diag[m_0, m_1, m_2, ..., m_n]$. The damping and stiffness matrices are as follows:

$$\mathbf{C} = \begin{bmatrix} c_{1,s} & -c_{1,s} & & & & \mathbf{O} \\ -c_{1,s} & c_{1,s}+c_{2,s} & -c_{2,s} & & & \\ & & \ddots & & & \\ & & & -c_{n-1,s} & c_{n-1,s}+c_{n,s} & -c_{n,s} \\ \mathbf{O} & & & & -c_{n,s} & c_{n,s} \end{bmatrix}, \tag{16}$$

$$\mathbf{K} = \begin{bmatrix} k_0 + k_{1,s} & -k_{1,s} & & & & \mathbf{O} \\ -k_{1,s} & k_{1,s} + k_{2,s} & -k_{2,s} & & & \\ & & \ddots & & & \\ & & & -k_{n-1,s} & k_{n-1,s} + k_{n,s} & -k_{n,s} \\ \mathbf{O} & & & & -k_{n,s} & k_{n,s} \end{bmatrix}. \tag{17}$$

The vectors $\boldsymbol{\phi_d} = [1, 0, \cdots, 0]^T_{(n+1)\times 1}$ and $\boldsymbol{\phi} = [1, 1, \cdots, 1]^T_{(n+1)\times 1}$ denote the coefficients of influence of the supplemental damping models and input seismic excitation, respectively. F_d is the force generated by RILD, LVD, INSTMW, or TMW, which is expressed as follows:

[**RILD**].

$$F_d = \eta k_0 \hat{x}_0(t) \tag{18}$$

[**LVD**],

$$F_d = \eta \mathrm{M}_{\mathrm{total}} \omega_0 \dot{x}_0 \tag{19}$$

[**INSTMW**].

$$F_d = m_d \ddot{x}_0 + k_n x_0 + \sum_{j=1}^{3} {}_j c_d \dot{x}_{d\,j} \tag{20}$$

$${}_j c_d \dot{x}_{d\,j} = {}_j k_d (x_0 - x_{d\,j}), \quad (j = 1, 2, 3) \tag{21}$$

[**TMW**],

$$F_d = \sum_{j=1}^{3} {}_j c_{d\,t}\ \dot{x}_{d\,j} \tag{22}$$

$${}_j c_{d\,t} \dot{x}_{d\,j} = {}_j k_{d\,t} (x_0 - x_{d\,j}), \quad (j = 1, 2, 3) \tag{23}$$

where $\mathrm{M}_{\mathrm{total}} = m_0 + \sum_{i=1}^{n} m_i$ denotes the total mass of the isolated structure. ${}_j c_{d\,t}$ and ${}_j k_{d\,t}$ are the damping coefficient and stiffness in the jth branch of the TMW model, respectively, as shown in Fig. 7. Similarly, ${}_j c_d$ and ${}_j k_d$ are the damping coefficient and stiffness in the jth branch of the INSTMW model, respectively. ω_0 is the angular frequency of the entire system when the superstructure is considered a rigid body. $\hat{x}_0(t)$ denotes the Hilbert transform of $x_0(t)$.

Moreover, the term F_{HD} represents the resistive force generated by the HD that provides nonlinearity to the system and is expressed as

$$F_{\mathrm{HD}} = \begin{cases} \frac{F_y}{x_y}(x_0 - x_p), & |F_{\mathrm{HD}}| < F_y \\ \mathrm{sgn}(\dot{x}_0) F_y, & |F_{\mathrm{HD}}| = F_y \end{cases} \tag{24}$$

where x_p denotes the plastic deformation of the HD. When HD is incorporated, $\boldsymbol{\phi_h} = [1, 0, \cdots, 0]^T_{(n+1)\times 1}$. Otherwise, $\boldsymbol{\phi_h} = \mathbf{0}_{(n+1)\times 1}$;

The equations of motion are integrated into the frequency domain for a system containing RILD because of its noncausality. Otherwise, Newmark's β method ($\beta = 1/4$) was used as the integration scheme.

4.4. Linear base-isolation system

The target loss factor η for all damping systems was set to 0.4, following the common design practices for base-isolated buildings in Japan. The coefficients of the RILD and LVD models were obtained using equations (1) and (19), respectively.

It is worth mentioning that a model with as few branches as feasible that achieves satisfactory performance is preferable in practice. Following the recommendation presented in Section 3.4, three branches of Maxwell elements can achieve practically constant loss stiffness over a specified frequency range (Fig. 6(a)). Therefore, a TMW model with three branches was considered, and the target angular frequency range was set to [0.5, 50] rad/s, which encompasses the first five eigenmodes. The parameters of the three Maxwell elements can be determined using the optimization method introduced in Section 3.3. The PSO parameters are listed in Table 1. Then, for an INSTMW model, the inertance and negative stiffness are determined such that the storage stiffness of the INSTMW is zero at the first two natural frequencies (i.e., $\hat{\omega}_1 = 1.57$ rad/s and $\hat{\omega}_2 = 13.57$ rad/s). Table 6 summarizes the parameters of the four damping models.

4.4.1. Frequency domain analysis

The performance of the damping models was first compared in the frequency domain in terms of the transfer functions and response power spectral densities (PSDs). Thus far, the 1995 Kobe N–S record was used as the input ground motion. Fig. 9 depicts the Fourier amplitude spectrum and PSD. The frequency responses of the isolator displacement and floor response acceleration at the rooftop and the damping force coefficient (damping force divided by the total weight of the base-isolated structure) of the corresponding response PSDs (the product of the square of the transfer functions and the PSD of the 1995 Kobe N–S record) are shown in Fig. 10.

As shown in Figs. 10(a) and (c), the squares of the displacement and damping force transfer functions of the INSTMW system are greater than those of the LVD and RILD systems in the angular frequency range below ω_0, which is attributed mainly to the negative stiffness element.

Table 6: Properties of the damping models (target loss factor $\eta = 0.4$)

Model	m_d (ton)	k_n (kN/m)	${}_1k_d$ (kN/m)	${}_2k_d$ (kN/m)	${}_3k_d$ (kN/m)	${}_1c_d$ (kN·s/m)	${}_2c_d$ (kN·s/m)	${}_3c_d$ (kN·s/m)
INSTMW	34	-4178	7226	4561	6319	5422	455	105
TMW	–	–						
LVD	damping coefficient (kN·s/m)							
	$\eta \mathrm{M}_{\mathrm{total}} \omega_0 = 2686$							
RILD	complex-valued stiffness (kN/m)							
	$i\eta k_0 = 4221i$							

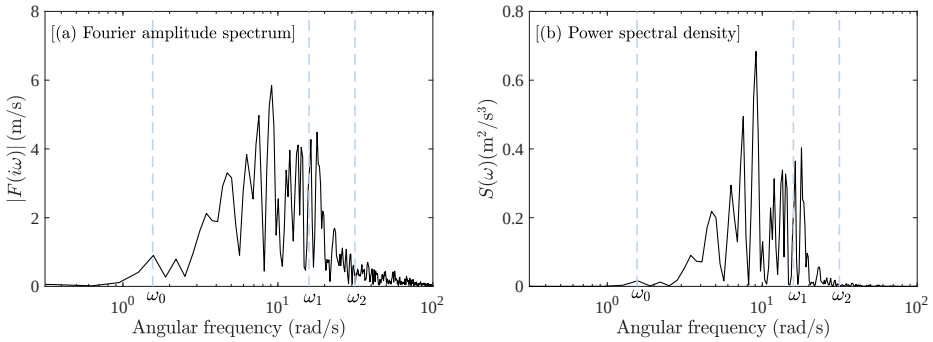

Figure 9: Fourier amplitude and PSD of the 1995 Kobe N–S record

Under the same loss factor, the damping forces of the INSTMW, LVD, and RILD systems are similar near ω_0; thus, their response displacement PSDs are comparable, suggesting that these systems yield similar displacement responses.

Nonetheless, the rooftop floor response acceleration PSD of the LVD system was significantly greater than that of the other systems around the second natural frequency, as shown in Fig. 10(e). This is attributed to the high acceleration transmissibility of the LVD system and the ground acceleration components in the vicinity of the second mode, as shown in Figs. 10(b) and 9(b). The first modal frequency of the TMW system was shifted to the right owing to the added storage stiffness, whereas the negative stiffness and inerter remained unchanged in the INSTMW system.

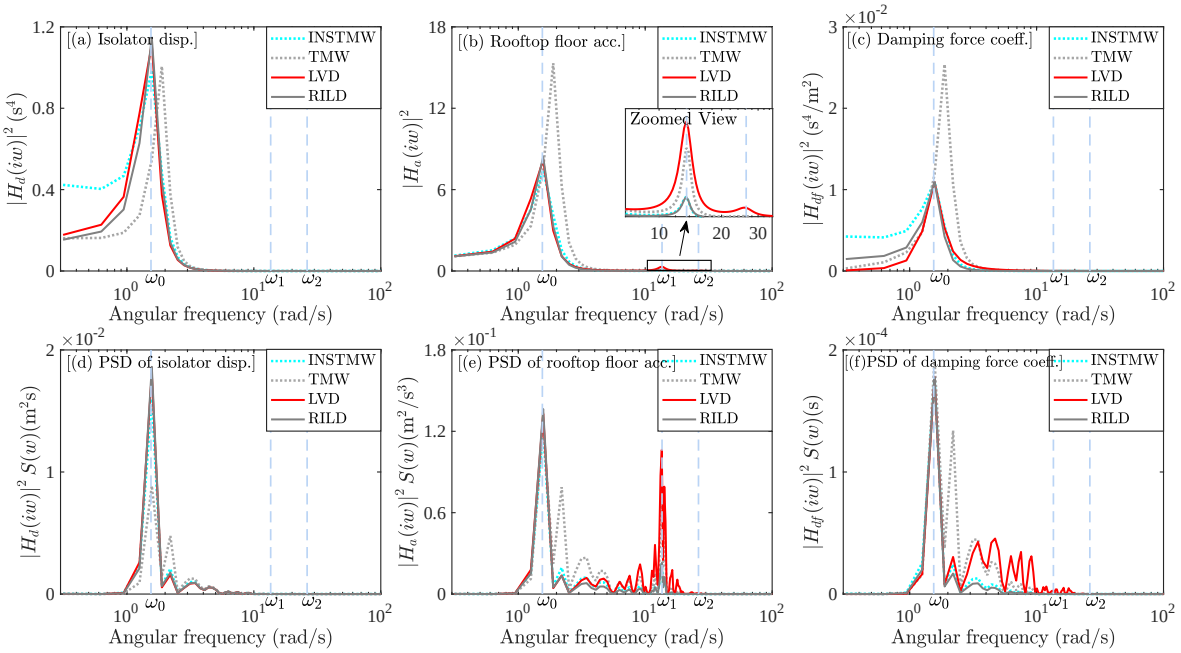

Figure 10: Transfer function and power spectral density (1995 Kobe N–S record)

The response PSDs shown in Figs. 10(d)–(f) demonstrate that the INSTMW system performs as well as the RILD system in suppressing the floor response acceleration and damping force without compromising the isolator displacement.

4.4.2. Response time-histories

The seismic performances of the INSTMW, TMW, LVD, and noncausal RILD models incorporated into the linear base-isolated structure were compared in terms of the relative isolator displacement, absolute rooftop floor acceleration, inter-story drift, and energy response history, as shown in Figs. 11, 13 and 14. Fig. 12 shows the hysteresis loops of the four damping models under input seismic records. Newmark's β method ($\beta = 1/4$) was used as the numerical integration scheme for the LVD, INSTMW, and TMW systems, whereas frequency domain analysis was conducted for the RILD system because of its non-causality.

As depicted in Fig. 11(a), the isolator displacement response histories of the INSTMW, LVD, and RILD systems were similar under the four input ground motions. This is because they are designed based on the same loss factor and thus have a comparable damping force near the first

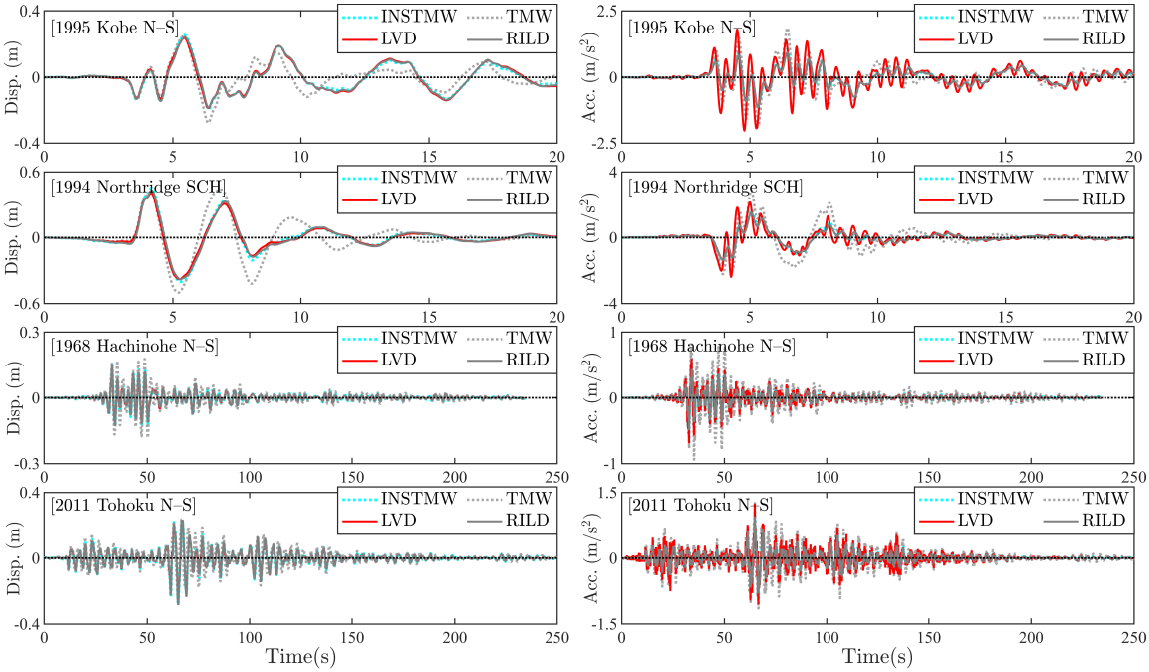

(a) Isolator displacement (b) Rooftop floor response acceleration

Figure 11: Displacement and rooftop floor acceleration response histories of linear base-isolated structures

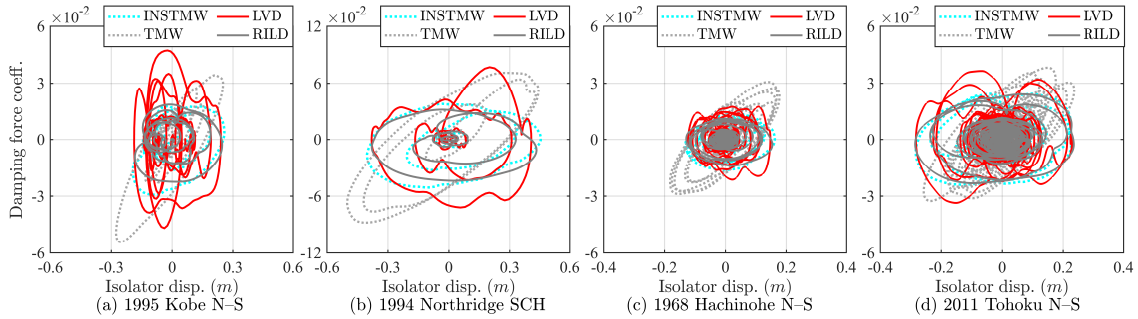

(a) 1995 Kobe N–S (b) 1994 Northridge SCH (c) 1968 Hachinohe N–S (d) 2011 Tohoku N–S

Figure 12: Hysteresis loops of different damping models in conjunction with linear base-isolated structures

structural mode that dominates the structural displacement response.

Conversely, the rooftop floor response accelerations yielded by the LVD model were substantially higher than those of the INSTMW and RILD models when subjected to the 1995 Kobe N–S and 1994 Northridge SCH records. This is attributed to the excessively large damping force induced by the high-frequency component in these two ground motions and the high acceleration transmissibility

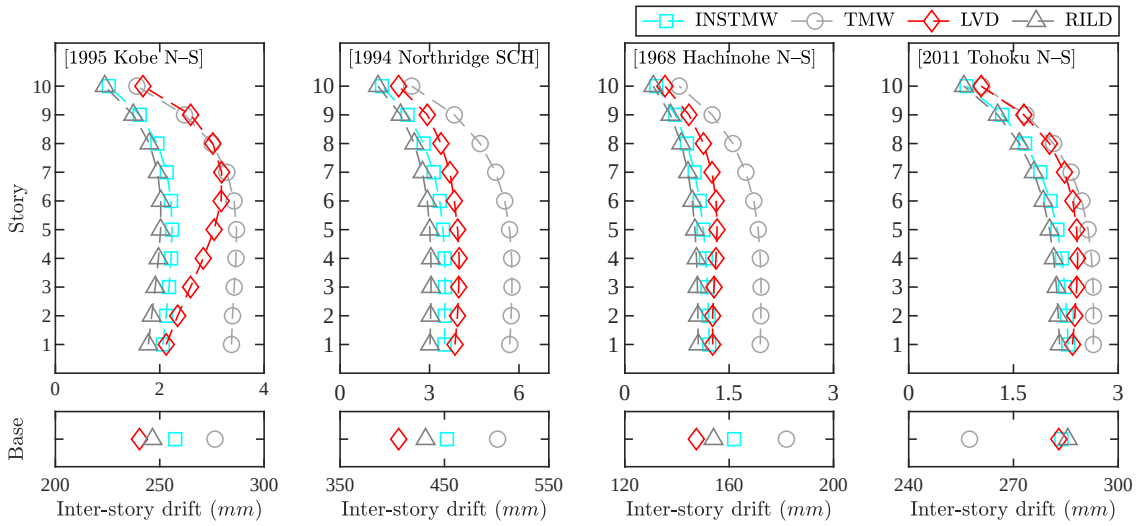

Figure 13: Inter-story drifts of linear base-isolated structures

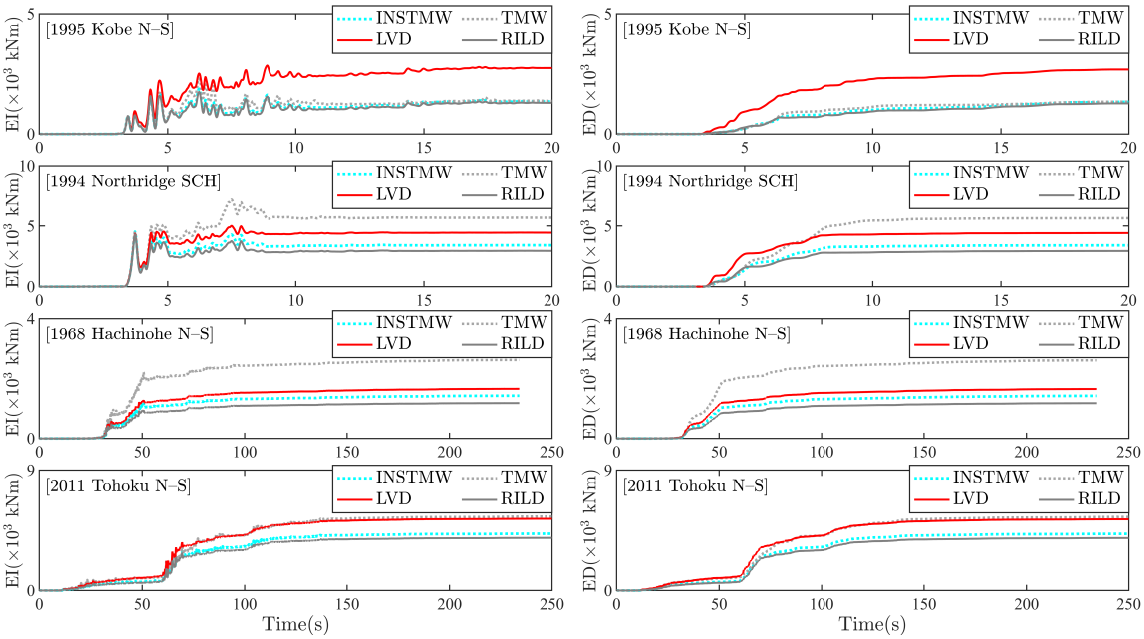

Figure 14: Energy response histories of linear base-isolated structures

near the second structural mode, as shown in Figs. 10 (b) and 12. Fig. 13 demonstrates that the INSTMW device achieves inter-story drifts comparable to those of RILD, outperforming the

LVD and TMW models. Although the large damping force generated by the LVD can dissipate a substantial amount of seismic energy, it results in a large seismic energy input to the structural system, as shown in Fig. 14.

The ability of the INSTMW model to suppress the control force while maintaining the isolator displacement control effect is evident when the model is subjected to earthquakes dominated by high frequencies (1995 Kobe N–S and 1994 Northridge SCH), as shown in Figs. 12(a) and (b). The INSTMW model cuts off high-frequency components that generate a high control force while barely contributing to the displacement response. In contrast, when subjected to earthquakes containing abundant low-frequency components (1968 Hachinohe N–S and 2011 Tohoku N–S), the benefit diminishes, as shown in Figs. 12(c) and (d).

Moreover, in Fig. 12, although both the TMW and INSTMW systems are designed to achieve constant loss stiffness in the specified frequency range, their hysteresis loops appear different owing to the differences in their storage stiffness. By adding the negative stiffness and inerter used in the INSTMW system, the RILD hysteresis loop can be successfully reproduced.

Although the TMW system is designed such that its loss stiffness is close to that of RILD in the specified angular frequency range, its maximum response displacement and floor response acceleration are the largest among the four damping systems under input excitation(except for 2011 Tohoku N–S). In addition, the inter-story drifts were significantly larger than those of the other damping models. In contrast, the response control performance of the INSTMW system is comparable to that of an RILD system, highlighting the importance of adjusting the loss and storage stiffness.

In conclusion, the INSTMW system benefits base-isolated structures by reducing the response displacement, floor response acceleration, inter-story drifts, and seismic energy input to a greater extent than the LVD system when subjected to ground motion dominated by frequencies higher than the fundamental natural frequency. The proposed system is never outperformed by the LVD and TMW systems if the dominant excitation frequency is higher than the fundamental natural frequency, which is ensured by designing the isolation frequency to be lower than the dominant frequency of excitation. Adjusting the storage stiffness is crucial for achieving a response control performance similar to that of an ideal RILD system. Using negative stiffness, an inerter is a viable and efficient option for adjusting the storage stiffness.

4.5. Nonlinear base-isolation system

This section considers a hybrid isolation system operating with an HD and linear damping system. With respect to linear damping systems, the INSTMW, TMW, and LVD models were employed, and their properties were the same as those listed in Table 6. For simplicity, hybrid damping systems that combine HD with the INSTMW, TMW, and LVD models are designated as H-INSTMW, H-TMW, and H-LVD, respectively. The notations HD-1, HD-2, and HD-3 in the plots represent the damping force of HD in the H-INSTMW, H-TMW, and H-LVD systems, respectively. The analysis is conducted in the time domain because of nonlinearity.

Fig. 15 plots the displacement and acceleration response time histories of nonlinear base-isolated structures equipped with different hybrid control systems subjected to four seismic records. Figs. 16 and 17 show the hysteresis loops of supplemental damping models and HDs, respectively. The inter-story drift of the superstructure is shown in Fig. 18.

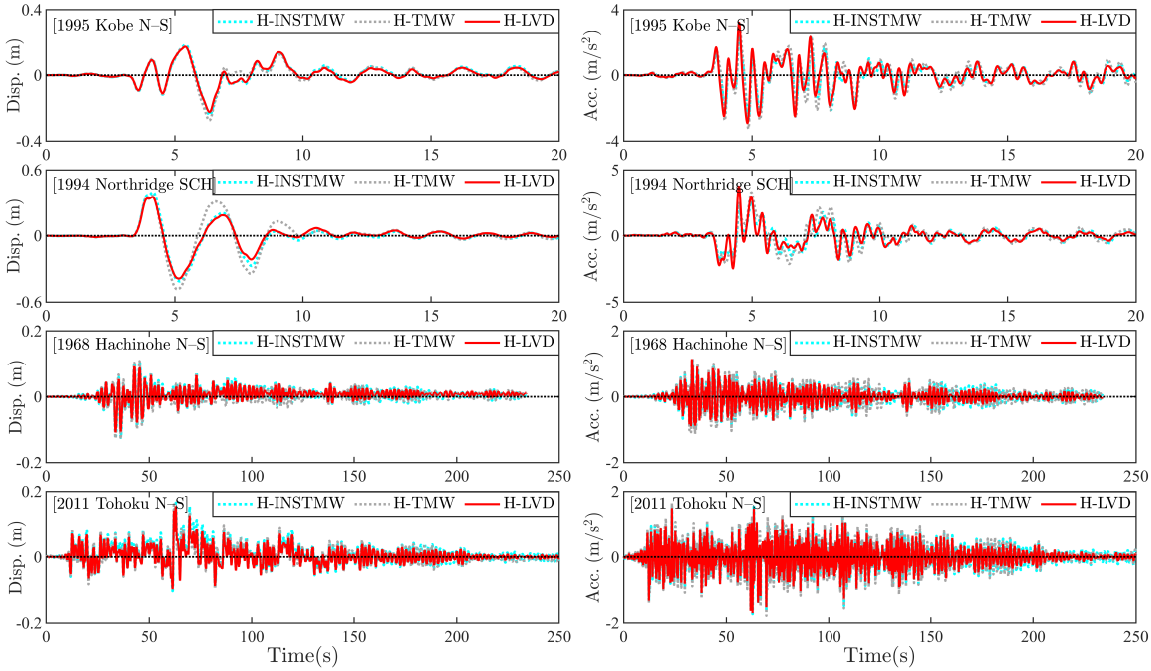

(a) Isolator displacement (b) Rooftop floor response acceleration

Figure 15: Displacement and rooftop floor acceleration response histories of nonlinear base-isolated structures

It is observed that H-INSTMW yields similar displacement response time histories to those of the H-LVD, whereas its maximum accelerations (see Table 7) and inter-story drifts of the superstructure

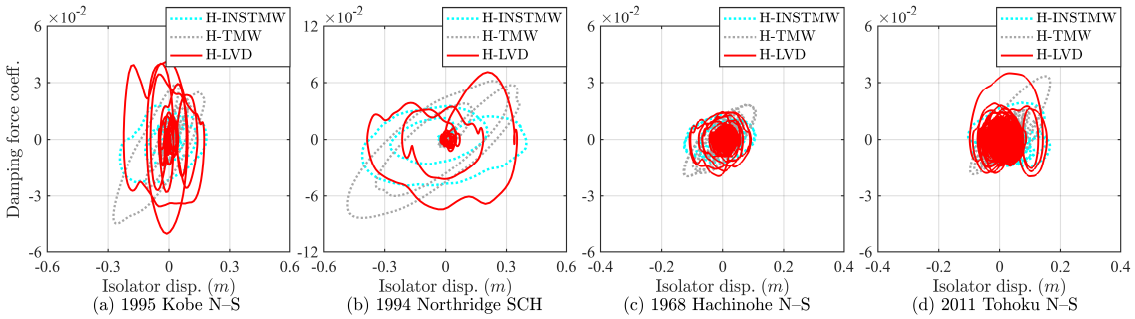

Figure 16: Hysteresis loops of damping models in conjunction with nonlinear base-isolated structures

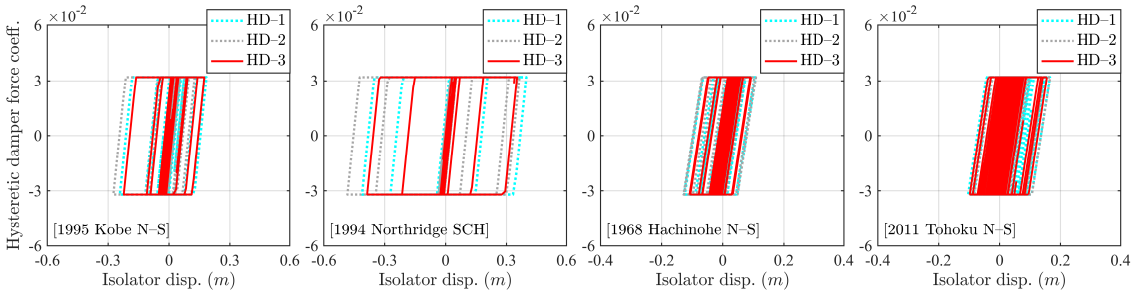

Figure 17: Hysteresis loops of HDs

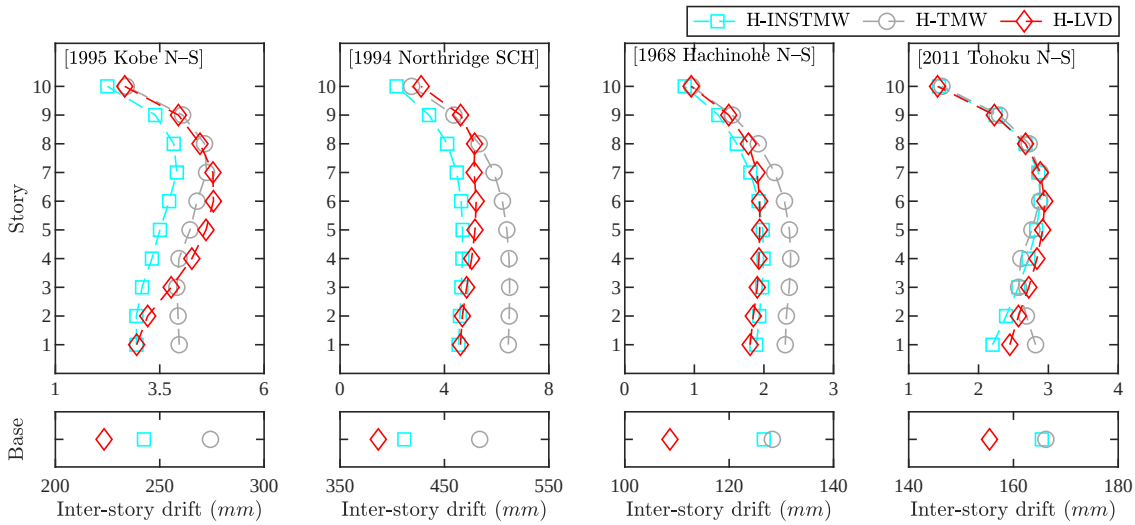

Figure 18: Inter-story drifts of nonlinear base-isolated structures

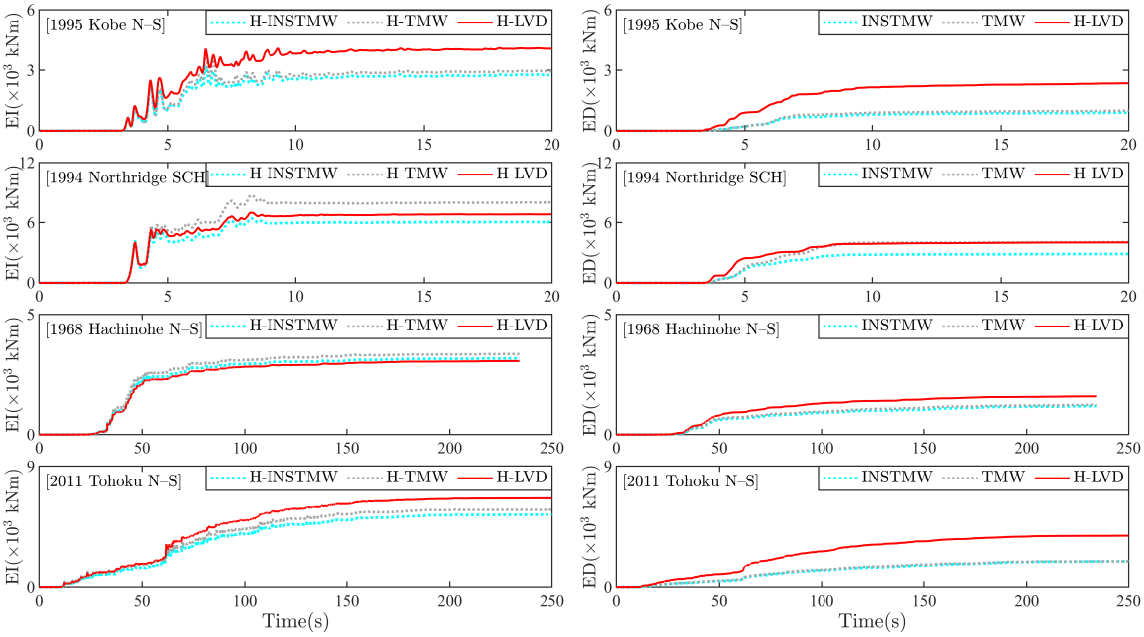

Figure 19: Energy response histories of nonlinear base-isolated structures

are lower than those of the H-LVD under the 1995 Kobe N–S and 1994 Northridge SCH records, as shown in Figs. 15 and 18. This is because the damping forces generated by the proposed model are lower, whereas the maximum resistive forces yielded by the HDs are the same, as shown in Figs. 16 and 17. Moreover, the INSTMW model dissipates less energy because of its lower damping forces, which also introduces less seismic energy to base-isolated structures than LVD, as shown in Fig. 19.

The ability of the INSTMW system to suppress the control force while maintaining the isolator displacement control effect in a nonlinear system is evident when the system is subjected to earthquakes dominated by high frequencies (1995 Kobe N–S and 1994 Northridge SCH), as shown in Figs. 16(a) and (b), whereas the benefit diminishes when it is subjected to earthquakes dominated by low-frequency components (1968 Hachinohe N–S and 2011 Tohoku N–S), as shown in Figs. 16(c) and (d).

To quantitatively compare the seismic responses yielded by different damper systems incorporated into linear and nonlinear isolation systems, Table 7 summarizes the maximum displacement and floor response acceleration values, in which the percentages of reduction of each response value compared with the LVD are shown in parentheses.

Table 7: Maximum response values of linear and nonlinear base-isolation systems

System	Seismic records	Max isolator displacement (m)				Max rooftop floor acceleration (m/s^2)			
		INSTMW	TMW	LVD	RILD	INSTMW	TMW	LVD	RILD
Linear case	1995 Kobe N–S	0.25(+4.2%)	0.28(+16.7%)	0.24	0.25(+4.2%)	1.23(-39.4%)	1.88(-7.4%)	2.03	1.14(-40.8%)
	1994 Northridge SCH	0.45(+9.7%)	0.50(+22.0%)	0.41	0.43(+4.9%)	1.69(-29.3%)	2.88(+20.5%)	2.39	1.53(-36.0%)
	1968 Hachinohe N–S	0.16(+6.7%)	0.18(+20.0%)	0.15	0.15(0)	0.54(-22.9%)	0.94(+34.3%)	0.70	0.49(-30.0%)
	2011 Tohoku N–S	0.28(0)	0.26(-7.1%)	0.28	0.29(+3.6%)	1.00(-20.0%)	1.26(+0.8%)	1.25	0.95(-24.0%)
Nonlinear case	1995 Kobe N–S	0.24(+9.1%)	0.27(+22.7%)	0.22	—	2.72(-15.5%)	3.25(+0.9%)	3.22	—
	1994 Northridge SCH	0.41(+5.1%)	0.49(+25.6%)	0.39		2.60(-30.7%)	3.30(-12.0%)	3.75	
	1968 Hachinohe N–S	0.13(+18.2%)	0.13(+18.2%)	0.11		1.03(-10.4%)	1.12(-2.6%)	1.15	
	2011 Tohoku N–S	0.17(+6.3%)	0.17(+6.3%)	0.16		1.72(+0.6%)	1.78(+4.1%)	1.71	

Evidently, the best performance in mitigating the isolated structural response is attained by RILD, which is incorporated into a linear isolation system that achieves similar displacement reductions with significantly lower response accelerations compared to LVD, particularly under the 1995 Kobe N–S and 1994 Northridge SCH cases. Similar results were observed for the INSTMW model, proving that the proposed model can causally realize the benefits of RILD. The performance improvement of the proposed system is attributed to the introduction of negative stiffness and inerter elements.

Specifically, compared with the LVD model under the 1995 Kobe N–S and 1994 Northridge SCH records, the floor response acceleration reductions of the INSTMW model were approximately 39% and 29% in the linear case and approximately 16% and 30% in the nonlinear case, respectively, with a slight increase in isolator displacements. Under the other two ground motions containing abundant low-frequency components, the floor response acceleration reductions were approximately 20% in the linear case, with similar displacement responses. Its control effects are less effective when applied to a nonlinear isolation system, particularly under the 2011 Tohoku N–S record.

For a linear base-isolation system, the numerical analysis results demonstrated the superiority of the proposed system over the TMW and LVD models in controlling displacement with lower demand for control force and reduced response indicators regarding floor response acceleration, inter-story drift, and earthquake energy input when subjected to ground motions dominated by high-frequency components. The results obtained from the nonlinear system demonstrate that the proposed system outperforms the TMW model. Compared with LVD, further challenges are identified for the proposed system in mitigating the responses of the isolated structure with nonlinearity

when subjected to ground motions containing abundant low-frequency components.

5. Conclusions

RILD benefits low-frequency structures by performing selective damping in the low-frequency region, particularly at the fundamental natural frequency of the structure, to effectively suppress response displacements while cutting off the high-frequency components responsible for undesirable large floor response accelerations.

The noncausality of RILD hinders its realization as a mechanical device to exploit this benefit. Causal approximation methods of RILD in the literature have focused on achieving constant loss stiffness and paid less attention to storage stiffness. A causal constant-loss stiffness model can be achieved at the expense of adding an undesirable storage stiffness proportional to the logarithm of the frequency.

Biot's model is the most successful in approximating the constant-loss stiffness characteristics of RILD, particularly in the high-frequency region. However, it requires infinite branches of Maxwell elements, making it impossible to realize it as a mechanical device. The TMW model is the most viable option for realizing RILD among the known causal RILD models because it can achieve practically sufficient accuracy in achieving constant loss stiffness within the specified target frequency with finite branches of Maxwell elements. Questions remain regarding the number of branches required and the method used to eliminate the undesirable storage stiffness added to the isolation layer.

To address the former question, a series of optimum designs was conducted to determine the relaxation parameters for Maxwell elements by varying the number of branches and the target frequency range in which constant loss stiffness is achieved. The results show that three branches enable the TMW model to achieve practically sufficient accuracy. The latter question is addressed using negative stiffness and inerter elements. Combining these two elements with different frequency dependencies allows us to adjust the isolator stiffness to exactly what we desire at least two independent frequencies.

Linear simulation analyses using a 10-story base-isolated structure model demonstrated that the proposed INSTMW model outperformed the LVD and TMW models in reducing the floor response acceleration and inter-story drifts while maintaining the isolator displacement control effect when subjected to ground motions dominated by high-frequency components and its seismic performance

was not compromised even when excited by ground motions containing abundant low-frequency components. Furthermore, an HD that remained elastic for a 500-year wind load return period was incorporated into the isolation layer to examine the performance of the proposed model when incorporated into a more realistic nonlinear isolation system. The results demonstrated that the proposed model outperformed the TMW model, whereas floor response acceleration reduction was achieved at the expense of compromised isolator displacement compared to LVD.

In the future, we plan to design and manufacture a full-scale prototype of the proposed device and conduct a full-scale dynamic validation test to study the potential application of the device to real-life building structures.

Acknowledgments

This work was supported by the Support for Pioneering Research Initiated by the Next Generation Program (Grant Number JPMJSP2114), provided by the Japan Science and Technology Agency. We would like to thank Editage (http://www.editage.com) for editing and reviewing this manuscript for the English language.

References

[1] I. Takewaki, S. Murakami, K. Fujita, S. Yoshitomi, M. Tsuji, The 2011 off the pacific coast of tohoku earthquake and response of high-rise buildings under long-period ground motions, Soil Dynamics and Earthquake Engineering 31 (11) (2011) 1511–1528. doi:10.1016/j.soildyn.2011.06.001.

[2] Y. Yu, S. Royel, Y. Li, J. Li, A. M. Yousefi, X. Gu, S. Li, H. Li, Dynamic modelling and control of shear-mode rotational mr damper for mitigating hazard vibration of building structures, Smart Materials and Structures 29 (11) (2020) 114006.

[3] R. E. D. Bishop, The treatment of damping forces in vibration theory, The Aeronautical Journal 59 (539) (1955) 738–742. doi:10.1017/S0368393100117122.

[4] T. Reid, Free vibration and hysteretic damping, The Aeronautical Journal 60 (544) (1956) 283–283. doi:10.1017/S0368393100135242.

[5] P. Lancaster, Free vibration and hysteretic damping, The Aeronautical Journal 64 (592) (1960) 229–229. doi:10.1017/S0368393100072515.

[6] S. Crandall, The hysteretic damping model in vibration theory, Proceedings of the Institution of Mechanical Engineers, Part C: Mechanical Engineering Science 205 (1) (1991) 23–28. doi:0.1243/PIME_PROC_1991_205_086_02.

[7] H. Luo, K. Ikago, C. Chong, A. Keivan, B. Phillips, Performance of low-frequency structures incorporated with rate-independent linear damping, Engineering Structures 181 (2019) 324–335. doi:10.1016/j.engstruct.2018.12.022.

[8] T. Caughey, Vibration of dynamic system with linear hysteretic damping (linear theory), in: Proc. of 4th US National Congress of Applied Mechanics, 1962, Vol. 1, ASCE, 1962, pp. 87–97.

[9] G. Muscolino, A. Palmeri, F. Ricciardelli, Time-domain response of linear hysteretic systems to deterministic and random excitations, Earthquake Engineering & Structural Dynamics 34 (9) (2005) 1129–1147. doi:10.1002/eqe.471.

[10] K. Ikago, N. Inoue, Behavior of rate-independent linear damping incorporated into long-period structures subjected to strong ground motions, in: Proceedings of the 6th World Conference on Structural Control and Monitoring, 2014, pp. 1116–1124.

[11] S. H. Crandall, Dynamic response of systems with structural damping, Tech. rep. (1961).

[12] J. A. Inaudi, J. M. Kelly, Linear hysteretic damping and the hilbert transform, Journal of Engineering Mechanics 121 (5) (1995) 626–632. doi:10.1061/(ASCE)0733-9399(1995)121:5(626).

[13] M. A. Biot, et al., Linear thermodynamics and the mechanics of solids, in: Proceedings of the Third US National Congress of Applied Mechanics, American Society of Mechanical Engineers, 1958.

[14] N. Makris, J. Zhang, Time-domain viscoelastic analysis of earth structures, Earthquake Engineering & Structural Dynamics 29 (6) (2000) 745–768. doi:10.1002/(SICI)1096-9845(200006)29:6<745::AID-EQE937>3.0.CO;2-E.

[15] P. D. Spanos, S. Tsavachidis, Deterministic and stochastic analyses of a nonlinear system with a biot visco-elastic element, Earthquake Engineering & Structural Dynamics 30 (4) (2001) 595–612. doi:10.1002/eqe.29.

[16] A. Reggio, M. De Angelis, R. Betti, A state-space methodology to identify modal and physical parameters of non-viscously damped systems, Mechanical Systems and Signal Processing 41 (1-2) (2013) 380–395.

[17] N. Makris, Causal hysteretic element, Journal of Engineering Mechanics 123 (11) (1997) 1209–1214. doi:10.1061/(ASCE)0733-9399(1997)123:11(1209).

[18] G. Muravskii, Linear models with nearly frequency independent complex stiffness leading to causal behaviour in time domain, Earthquake Engineering & Structural Dynamics 36 (1) (2007) 13–33. doi:10.1002/eqe.607.

[19] N. Nakamura, Practical causal hysteretic damping, Earthquake Engineering & Structural Dynamics 36 (5) (2007) 597–617. doi:10.1002/eqe.644.

[20] Y. Huang, R. Sturt, M. Willford, A damping model for nonlinear dynamic analysis providing uniform damping over a frequency range, Computers & Structures 212 (2019) 101–109. doi:10.1016/j.compstruc.2018.10.016.

[21] G. Genta, N. Amati, On the equivalent viscous damping for systems with hysteresis, Atti della Accademia delle Scienze di Torino 32 (2009) 21–43.

[22] A. Keivan, B. M. Phillips, M. Ikenaga, K. Ikago, Causal realization of rate-independent linear damping for the protection of low-frequency structures, Journal of Engineering Mechanics 143 (9) (2017) 04017058. doi:10.1061/(ASCE)EM.1943-7889.0001259.

[23] W. Liu, K. Ikago, Feasibility study of a passive rate-independent damping device for the seismic protection of low-frequency structures, Structures 34 (2021) 2499–2514. doi:10.1016/j.istruc.2021.09.005.

[24] W. Liu, K. Ikago, Feasibility study of the physical implementation of rate-independent linear damping for the protection of low-frequency structures, Journal of Building Engineering 44 (2021) 103319. doi:10.1016/j.jobe.2021.103319.

[25] W. Liu, K. Ikago, Experimental study of earthquake input energy of low-frequency structures equipped with a passive rate-independent damping device, Structural Control and Health Monitoring 29 (2) (2021) e2883. doi:10.1002/stc.2883.

[26] W. Liu, K. Ikago, Performance of a passive rate-independent damping device in a seismically isolated multistory building, Structural Control and Health Monitoring 29 (6) (2022) e2941. doi:10.1002/stc.2941.

[27] W. Liu, K. Ikago, Feasibility of physical implementation of rate-independent linear damping to protect multistory low-frequency structures, Journal of Sound and Vibration 528 (2022) 116893. doi:10.1016/j.jsv.2022.116893.

[28] H. Luo, K. Ikago, Unifying causal model of rate-independent linear damping for effectively reducing seismic response in low-frequency structures, Earthquake Engineering & Structural Dynamics (2021). doi:10.1002/eqe.3450.

[29] S. Nakaminami, K. Ikago, N. Inoue, H. Kida, Response characteristics of a base-isolated structure incorporated with a force-restricted viscous mass damper, in: Proceedings of the 15th World Conference on Earthquake Engineering, Lisbon, Portugal, 2012, p. 0484.

[30] Y. Watanabe, K. Ikago, N. Inoue, H. Kida, S. Nakaminami, H. Tanaka, Y. Sugimura, K. Saito, Full-scale dynamic tests and analytical verification of a force-restricted tuned viscous mass damper, Proceedings of the 15th World Conference on Earthquake Engineering.

[31] A. Reggio, M. De Angelis, Modelling and identification of structures with rate-independent linear damping, Meccanica 50 (3) (2015) 617–632. doi:10.1007/s11012-014-0046-3.

[32] A. A. Sarlis, D. T. R. Pasala, M. Constantinou, A. Reinhorn, S. Nagarajaiah, D. Taylor, Negative stiffness device for seismic protection of structures, Journal of Structural Engineering 139 (7) (2013) 1124–1133. doi:10.1061/(ASCE)ST.1943-541X.0000616.

[33] H. Li, Y. Yu, J. Li, Y. Li, M. Askari, Multi-objective optimisation for improving the seismic protection performance of a multi-storey adaptive negative stiffness system based on modified nsga-ii with dcd, Journal of Building Engineering 43 (2021) 103145.

[34] T. Sun, Z. Lai, S. Nagarajaiah, H.-N. Li, Negative stiffness device for seismic protection of smart base isolated benchmark building, Structural Control and Health Monitoring 24 (11) (2017) e1968. doi:10.1002/stc.1968.

[35] W. Liu, K. Ikago, Z. Wu, I. Fukuda, Modified tuned maxwell–wiechert model for improving seismic performance of base-isolated structures, Journal of Building Engineering 54 (2022) (2021) 104616.

[36] C.-L. Lee, Proportional viscous damping model for matching damping ratios, Engineering Structures 207 (2020) 110178. doi:10.1016/j.engstruct.2020.110178.

[37] J. Kennedy, R. Eberhart, Particle swarm optimization, Proceedings of IEEE International Conference on Neural Networks IV (1995) 1942–1948. doi:10.1109/ICNN.1995.488968.

[38] Y. Shi, R. C. Eberhart, Parameter selection in particle swarm optimization, in: International conference on evolutionary programming, 1998, pp. 591–600. doi:10.1007/BFb0040810.

[39] M. R. Bonyadi, Z. Michalewicz, Particle swarm optimization for single objective continuous space problems: a review, Evolutionary computation 25 (1) (2017) 1–54. doi:10.1162/EVCO_r_00180.

[40] Y. Yu, A. N. Hoshyar, H. Li, G. Zhang, W. Wang, Nonlinear characterization of magnetorheological elastomer-based smart device for structural seismic mitigation, International Journal of Smart and Nano Materials 12 (4) (2021) 390–428.

[41] K. L. Ryan, J. Polanco, Problems with rayleigh damping in base-isolated buildings, Journal of Structural Engineering 134 (11) (2008) 1780–1784.

[42] H. Anajafi, R. A. Medina, E. Santini-Bell, Effects of the improper modeling of viscous damping on the first-mode and higher-mode dominated responses of base-isolated buildings, Earthquake Engineering & Structural Dynamics 49 (1) (2020) 51–73.